Spatially twisted liquid-crystal devices ⊞

Alicia Sit ⓘ ; Francesco Di Colandrea ⓘ ; Alessio D'Errico ⓘ ; Ebrahim Karimi ✉ ⓘ

🅡 Check for updates

🌐
View
Online

↗
Export
Citation

AIP Publishing

Spatially twisted liquid-crystal devices 🔵EP

View Online　　Export Citation　　CrossMark

Alicia Sit,[a) 🔵] Francesco Di Colandrea, [🔵] Alessio D'Errico, [🔵] and Ebrahim Karimi[b) 🔵]

AFFILIATIONS

Nexus for Quantum Technologies, University of Ottawa, Ottawa, Ontario K1N 5N6, Canada

[a)]**Current address:** National Research Council of Canada, 100 Sussex Drive, K1N 5A2, Ottawa, Ontario, Canada.
[b)]**Author to whom correspondence should be addressed:** ekarimi@uottawa.ca

ABSTRACT

Nematic liquid-crystal devices are a powerful tool to structure light in different degrees of freedom, both in classical and in quantum regimes. Most of these devices exploit the possibility of introducing a position-dependent phase retardation either with a homogeneous alignment of the optic axis—e.g., liquid-crystal-based spatial light modulators—or, conversely, with a uniform but tunable retardation and patterned optic axis, e.g., q-plates. The pattern is the same in the latter case on the two alignment layers. Here, a more general case is considered, wherein the front and back alignment layers are patterned differently. This creates a non-symmetric device, which can exhibit different behaviors depending on the direction of beam propagation and effective phase retardation. In particular, we fabricate multi-q-plates by setting different topological charges on the two alignment layers. The devices have been characterized by spatially resolved Stokes polarimetry, with and without applied electric voltage, demonstrating new functionalities.

INTRODUCTION

When nematic liquid crystals are placed between parallel glass plates with differing alignment directions, the bulk will twist in order to match the boundary conditions.[1] This phenomenon of a twisted nematic liquid-crystal (TNLC) cell—in particular with 90° twists—has been used extensively for the development of everyday liquid-crystal displays.[2–4] With properly chosen birefringent liquid crystals and fabrication techniques, incident linearly polarized light will rotate through the cell, following the twist structure. When a sufficiently strong voltage is applied across the cell, the twist structure disappears as the liquid crystals are aligned in the field direction, negating any polarization rotation. However, there has been limited study of the twisted cell beyond the 90° twist case for general polarization manipulation.[5,6]

Meanwhile, in the context of experimental optics, spatially patterned liquid-crystal-based devices are an efficient and compact method for structuring the polarization and spatial degrees of freedom of light, but studies have been limited to symmetric elements, i.e., the front and back patterns on the alignment layers are identical. For example, q-plates—part of the general class of Pancharatnam–Berry phase optical elements (PBOEs)—are such that the liquid-crystal layer is aligned to have a semi-integer topological charge of q—note that such a topological structure, similar to q-plates, may be formed by liquid crystal droplets.[7] This allows for the coupling of photonic spin to orbital angular momentum. q-plates have found applications in both classical and quantum optics,[8,9] in particular STED microscopy,[10] metrology,[11] high-dimensional classical[12] and quantum communication,[13] and quantum simulations.[14] For the case of non-symmetric spatially patterned devices, there have been only a few implementations, including polarization converters, which convert linear polarization into vector vortex modes,[15] a functionality still achievable via standard q-plates.[16] However, these spatially twisted elements operate with no externally applied field. Only recently, the voltage-dependent behavior of non-symmetric devices patterned with different gratings has been observed.[17–19] Similar investigations have been reported for other classes of materials.[20–22]

This article aims to bridge the above gaps by investigating the behavior of liquid crystals with the full range of possible twist angles from −90° to 90°, under the influence of externally applied electric fields. We first analyze the derived Jones matrix for a static TNLC cell, i.e., with no applied field, and discuss its expected behavior in the so-called adiabatic following regime for different effective phase retardations Γ. There is a potential dual behavior that a TNLC cell exhibits—which has not previously been reported—and it has wide-reaching implications for their spatially varying extensions. An incident circularly polarized beam may acquire three unique phase distributions from, respectively, $\Gamma = 0$, $\Gamma = \pi$, and $\Gamma = 0$ with reversed-plate orientation. Dual-plates (DPs), as we will call them, thus promise a switch-like capability between phase distributions.

07 December 2024 15:55:02

Moreover, an externally applied electric field ultimately enables a transition in the effective topological charge of generated polarization patterns. Proof-of-principle spatially twisted liquid-crystal devices are fabricated and compared with the above two case studies.

RESULTS

No applied field

A TNLC cell of thickness L without any externally applied field can be modeled as a stack of infinitely thin waveplates, which are gradually twisted from one to the next. With a total twist angle of α, and assuming strong anchoring, the twist distribution with propagation is linear, $\phi(z) = \alpha z/L$, where z is the axis normal to the cell.[23] For positively uniaxial nematic liquid crystals with extraordinary and ordinary refractive indices n_e and n_o, respectively, we can define the parameter $\Gamma = 2\pi(n_e - n_o)L/\lambda$ (λ is the wavelength of the incident light), which corresponds to the total phase retardation for a zero-twist cell. The Jones matrix describing the TNLC configuration, shown in Fig. 1(a), can be modeled as a stack of N thin waveplates, each possessing a phase retardation of Γ/N; the nth waveplate is rotated to be at an angle of $n\alpha/N$. By matrix multiplication, the total Jones matrix $\mathbf{T}_0(\alpha, \Gamma)$ is

$$\mathbf{T}_0(\alpha, \Gamma) = \prod_{n=1}^{N} \mathbf{R}(-n\alpha/N)\mathbf{W}_0(\Gamma/N)\mathbf{R}(n\alpha/N)$$
$$= \mathbf{R}(-\alpha)\{\mathbf{W}_0(\Gamma/N)\mathbf{R}(\alpha/N)\}^N, \tag{1}$$

where

$$\mathbf{W}_0(\Gamma) = \begin{bmatrix} e^{-i\frac{\Gamma}{2}} & 0 \\ 0 & e^{i\frac{\Gamma}{2}} \end{bmatrix}, \tag{2}$$

and the rotation matrix $\mathbf{R}(\cdot)$ is

$$\mathbf{R}(\cdot) = \begin{bmatrix} \cos(\cdot) & \sin(\cdot) \\ -\sin(\cdot) & \cos(\cdot) \end{bmatrix}. \tag{3}$$

The closed form of Eq. (1) in the limit as $N \to \infty$ simplifies to[23,24]

$$\mathbf{T}_0(\alpha, \Gamma) = \mathbf{R}(-\alpha)\begin{bmatrix} \cos X - \dfrac{i\Gamma}{2X}\sin X & \dfrac{\alpha}{X}\sin X \\ -\dfrac{\alpha}{X}\sin X & \cos X + \dfrac{i\Gamma}{2X}\sin X \end{bmatrix}$$
$$=: \mathbf{R}(-\alpha)\mathbf{M}_0(\alpha, \Gamma), \tag{4}$$

with $X = \sqrt{\alpha^2 + (\Gamma/2)^2}$. For the case where the fast axes of the front and back layers are aligned at angles ϕ_f and ϕ_b, respectively, the general twisted matrix, after setting $\alpha = \phi_b - \phi_f$, becomes

$$\mathbf{T}_{\phi_f}(\alpha, \Gamma) = \mathbf{R}(-\phi_f)\big[\mathbf{R}(\phi_f - \phi_b)\mathbf{M}_0(\alpha, \Gamma)\big]\mathbf{R}(\phi_f)$$
$$= \mathbf{R}(-\alpha)\mathbf{M}_{\phi_f}(\alpha, \Gamma), \tag{5}$$

with $\mathbf{M}_{\phi_f}(\alpha, \Gamma) = \mathbf{R}(-\phi_f)\mathbf{M}_0(\alpha, \Gamma)\mathbf{R}(\phi_f)$.

The optical action associated with Eq. (3) can be conveniently visualized on the Poincaré sphere (PS). We recall that the positive (negative) points of the three principal axes $\hat{S}_1$, $\hat{S}_2$, and $\hat{S}_3$ on the PS correspond to horizontal (vertical), diagonal (anti-diagonal), and right-hand circular (left-hand circular) polarization states. Figure 1(b) demonstrates the action of a TNLC cell on a horizontally polarized input for twist angles between $-\pi/2$ and $\pi/2$ and a global phase retardation of $\Gamma = \pi$. In this case, the output is always elliptical, wherein the handedness is determined by the sign of α.

Remarkably, if $\Gamma \gg \alpha$, then $\mathbf{M}_0(\alpha, \Gamma)$ simplifies to a waveplate $\mathbf{W}_0(\Gamma)$ with its fast axis along the horizontal, and Eq. (5) becomes

$$\mathbf{T}_{\phi_f}(\alpha, \Gamma) \approx \mathbf{R}(-\alpha)\mathbf{W}_{\phi_f}(\Gamma), \tag{6}$$

where $\mathbf{W}_{\phi_f}(\Gamma) = \mathbf{R}(-\phi_f)\mathbf{W}_0(\Gamma)\mathbf{R}(\phi_f)$ is a typical waveplate of retardance Γ, with fast axis oriented at ϕ_f. Consequently, an input beam that is linearly polarized either parallel or orthogonal to ϕ_f will be rotated by α in the counterclockwise direction. This is referred to as *adiabatic following* or the *Mauguin limit*. Figure 1(c) demonstrates this behavior for a horizontally polarized input state for a range of twist angles, wherein the output states are calculated via Eq. (3) with $\Gamma = 1001\pi$. The horizontal input—parallel to the input
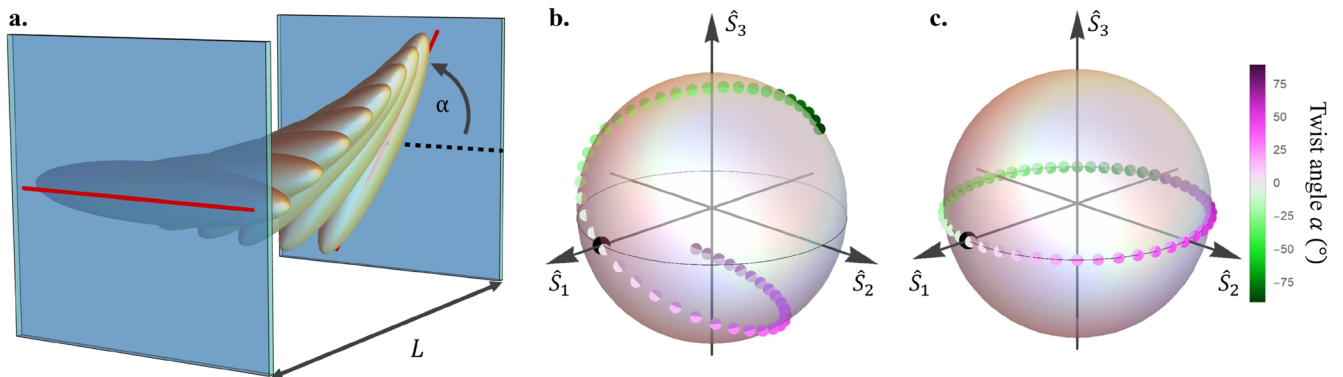
FIG. 1. Twisted nematic liquid-crystal cells. (a) Illustration of liquid crystals twisting between two glass plates, uniformly aligned at 0° and α for the front and back layers, respectively, spaced apart by a distance of L. The action of this configuration is shown on the Poincaré sphere on a horizontally polarized input state (black dot) for varying twist angles α between $-\pi/2$ and $+\pi/2$, with a birefringence of (b) $\Gamma = \pi$ and (c) $\Gamma = 1001\pi$ in the adiabatic following regime.

07 December 2024 15:55:02

alignment layer—is rotated by α toward other linear states along the equator of the PS.

Furthermore, the effective phase retardation is defined modulo 2π [see Eq. (5)]. Accordingly, Eq. (6) simplifies further for two cases: $\Gamma \ (\text{mod } 2\pi) = 0$ and $\Gamma \ (\text{mod } 2\pi) = \pi$. For $\Gamma \ (\text{mod } 2\pi) = 0$, $\mathbf{W}_{\phi_f}(0)$ reduces to the identity matrix, leaving

$$\mathbf{T}_{\phi_f}(\alpha, 0) = \begin{bmatrix} \cos \alpha & -\sin \alpha \\ \sin \alpha & \cos \alpha \end{bmatrix}. \qquad (7)$$

The left-handed (L) and right-handed (R) circular polarizations are rotation-invariant states (up to a global phase), so explicitly acting this on the circular basis yields $\{|L\rangle, |R\rangle\} \rightarrow \{e^{-i\alpha}|L\rangle, e^{i\alpha}|R\rangle\}$, where we have adopted the bra–ket notation to denote the complex polarization spinor. For the case where $\Gamma \ (\text{mod } 2\pi) = \pi$, Eq. (6) simplifies to

$$\mathbf{T}_{\phi_f}(\alpha_\pi, \pi) = \begin{bmatrix} \cos \alpha_\pi & \sin \alpha_\pi \\ \sin \alpha_\pi & -\cos \alpha_\pi \end{bmatrix}, \qquad (8)$$

with $\alpha_\pi = \phi_b + \phi_f$. This is the Jones matrix for a half-wave plate oriented at $\alpha_\pi/2$, yielding $\{|L\rangle, |R\rangle\} \rightarrow \{e^{i\alpha_\pi}|R\rangle, e^{-i\alpha_\pi}|L\rangle\}$. Of course, we can also consider the case for an arbitrary Γ. In this case, Eq. (6) can be rewritten explicitly as follows:

$$\mathbf{T}_{\phi_f}(\alpha, \Gamma) = \frac{(1 + e^{i\Gamma})}{2}\mathbf{T}_{\phi_f}(\alpha, 0) + \frac{(1 - e^{i\Gamma})}{2}\mathbf{T}_{\phi_f}(\alpha_\pi, \pi). \qquad (9)$$

The general case is, therefore, a superposition of the cases $\Gamma \ (\text{mod } 2\pi) = 0$ and $\Gamma \ (\text{mod } 2\pi) = \pi$, and the relative amplitudes are determined by the phase retardation.

In the following, we extend this analysis to spatially varying dual-plates, allowing for a spatial distribution of the fast-axis orientation of the front and back plates in the transverse plane, $\Phi_f(r, \varphi)$ and $\Phi_b(r, \varphi)$, respectively, described in cylindrical coordinates. An incident circularly polarized beam will acquire a spatially varying phase proportional to either $\alpha(r, \varphi) = \Phi_b(r, \varphi) - \Phi_f(r, \varphi)$ or $\alpha_\pi(r, \varphi) = \Phi_b(r, \varphi) + \Phi_f(r, \varphi)$, i.e., the difference or sum of the two fast axis distributions, depending on if $\Gamma \ (\text{mod } 2\pi) = 0$ or $\Gamma \ (\text{mod } 2\pi) = \pi$. Therefore, we can use the phase retardation of a dual-plate to toggle between two different behaviors. In addition, for a given dual-plate, if the front and back layers are reversed—i.e., the orientation of the plate is flipped, or the beam enters from the back—a distinct third phase pattern could be acquired at $\Gamma \ (\text{mod } 2\pi) = 0$, defined by $\alpha^{(-)} = \Phi_f - \Phi_b = -\alpha$. Of course, we could also consider the inverse problem wherein we desire a particular twist distribution; in this case, $\Phi_b = (\alpha_\pi + \alpha)/2$ and $\Phi_f = (\alpha_\pi - \alpha)/2$.

One potential challenge that arises when dealing with the general class of non-symmetric inhomogeneous liquid-crystal plates is that nematic liquid crystals only favorably twist between $-90°$ and $90°$. For example, if $\phi_f = 22.5°$ and $\phi_b = 157.5°$, then $\alpha = -45°$, and not $135°$, in order to achieve the lowest possible twist. At locations where ϕ_f and ϕ_b are orthogonal, there is an ambiguity as to whether $\alpha = +90°$ or $-90°$. This leads to discontinuities in the twist distribution, which results in π-phase jumps appearing in these locations. Consequently, a spatially varying global phase distribution will be imparted to any input beam, regardless of the birefringence setting.

An interesting example of a spatially varying dual-plate is the multi-q-plate. The functionality of a q-plate is equivalent to that of a half-wave plate with a fast-axis distribution of $\Phi_{QP}(\varphi) = q\varphi + \varphi_0$, where q, the topological charge of the plate, is either a full- or half-integer, and φ_0 is an offset angle. Its Jones matrix is identical to Eq. (8) with $\alpha_\pi = 2\Phi$, and the circularly polarized input will experience spin-to-orbital angular momentum coupling. For example, an input photon with a spin of $+(-)\hbar$ along the axis of propagation will gain $+(-)2q\hbar$ units of orbital angular momentum (OAM), where $\hbar$ is the reduced Planck constant, at the expense of switching the spin to be $-(+)\hbar$. We have adopted the convention that a spin of $+(-)\hbar$ corresponds to left (right) circularly polarized light. A q-plate can thus span the two-dimensional vector space $\{|R, 2q\rangle, |L, -2q\rangle\}$, where we have used the Dirac notation with the labels corresponding to a photon's polarization and OAM, respectively.

However, in order to have access to states created from a $-q$-plate—thus accessing a four-dimensional vector space—it is necessary to place a half-wave plate, or an equivalent device, to impart a $\lambda/2$ retardation, after the original q-plate. In addition, it is impossible to modify the topology of a q-plate once this is fabricated. An appropriately patterned dual-plate is capable of performing both of these tasks without the aid of additional optical elements. For example, define the front and back distributions to be $\Phi_f(\varphi) = q_f\varphi$ and $\Phi_b(\varphi) = q_b\varphi$, respectively (we have dropped the offset angles without loss of generality). If $q_f = q_b$, we straightforwardly recover the behavior of a regular $q = q_b$-plate so that we will assume $q_f \neq q_b$, and we get the following cases:

(1) If $q_f = 0$, then $\alpha = \alpha_\pi = q_b\varphi$, and we lose the dual behavior of the dual-plate.

(2) However, if $q_b = 0$, then $\alpha = -q_f\varphi$ and $\alpha_\pi = q_f\varphi$; we can thus use the phase retardation of the dual-plate to toggle between the behavior of oppositely charged q_f-plates. We note that cases (1) and (2) are the same dual-plates; however, the orientation of the device—or equivalently the beam propagation—is reversed. So, while we obtain two distinct behaviors through α and α_π, we do not gain a third behavior since $\alpha^{(-)} = \alpha$ in case (2).

(3) In general, if $|q_f|, |q_b| > 0$, then $\alpha \neq \alpha_\pi$ and $\alpha^{(-)} \neq \alpha$, thus creating a multi-q-plate with three possible behaviors. We note that the same concept can be applied to any phase distribution. Indeed, we are not limited to Φ_f and Φ_b being of the same class of phases. In this way, we can create arbitrary dual-functionality dual-setting devices.

To explore the validity of the TNLC model, several dual-plates are fabricated and then characterized using a 635-nm diode laser (see Materials and Methods). The first device is a discretized multi-q-plate DP($q_b = 0$, $q_f = 1/2$), with ~35 μm spacers, where DP stands for dual-plate, and the labels are the topologies of the front and back plate. Figure 2(a) shows the fabricated sample as it appears between crossed polarizers. The $q = 1/2$ topology is discretized into 16 slices such that a range of twist angles from $[-90°, 90°]$ can be efficiently characterized with enough room in each slice to average imperfections from the assemblage. The second sample fabricated and tested is a DP(1, 2), as shown in Fig. 2(b). The experimentally calculated average Stokes vectors for each of the 16 slices of
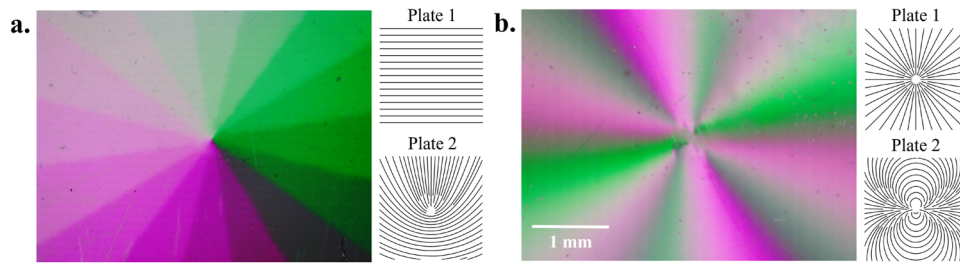
FIG. 2. Fabricated samples. False color images of (a) discretized DP(0, 1/2) and (b) DP(1, 2) between crossed polarizers under a microscope illuminated with white light. The topological pattern on each glass plate is also shown. Note that the $q = 1/2$ pattern is discretized into 16 slices for the patterning process.

DP(0, 1/2) with different input polarized light are plotted on the Poincaré sphere, along with theoretical fits [see Fig. 3(a)]. The results for DP(1/2, 0) are shown in Fig. 3(b). Figures 4(a) and 4(b) show the locally reconstructed Stokes vectors for horizontally polarized input light on DP(1, 2) and DP(2, 1), respectively. A very nice agreement is observed for the two cases, despite the singularity misalignment deriving from the fabrication process (see the supplementary material figures for a cross-sectional plot around the singularity).

The diameters of the spacers placed between the glass plates of the cell range from 32 to 38 μm, with an average of 35 μm. This gives our sample an average phase retardation of $\Gamma_{avg} = 51.7$ for 6CHBT liquid crystals with $\Delta n = 0.151.$[25] This Γ_{avg} is used when plotting the theoretical fits using the TNLC Jones matrix $\mathbf{T}_{\phi_f}(\alpha, \Gamma)$ of Eq. (4) in Figs. 3(a) and 3(b). As a measure of good fit, the average state overlap across all twist angles for a given input polarization is used. The overlap is calculated as $(1 + \mathbf{S}_{\exp} \cdot \mathbf{S}_{TNLC})/2$, where $\mathbf{S}_{\exp}$ and $\mathbf{S}_{TNLC}$ are the experimentally reconstructed and theoretical Stokes vectors, respectively. The uncertainties on each average Stokes vector are the standard deviations from the area used for averaging, which are less than 10% for each Stokes parameter in all cases. The theoretical fits using $\Gamma_{avg} = 51.7$ imitate the experimental data for all input polarizations and the two orientation cases very well, with total average

overlaps of 89% and 87% for DP(0, 1/2) and DP(1/2, 0), respectively. Deviations from theoretical predictions are mainly ascribed to fabrication defects. Higher-quality samples could be fabricated with the aid of microscopes and precision controls.

Externally applied field

When an electric voltage is applied across the DP(0, 1/2) sample, the resulting effect on polarized light can be surprising. Figure 5(a) shows the reconstructed local Stokes vectors at different voltages from a horizontally polarized input state. The color is encoded to show the azimuthal angle $\psi = \arctan(S_2/S_1)$ of the Stokes vectors on the Poincaré sphere. We experimentally observe that the overall topological charge can be tuned from $q \sim 1/2$ to $q \sim 1$ to $q \sim 0$ and back to $q \sim 1$ as we increase the field strength. While detuning to $q = 0$ is observed with standard q-plates, this apparent charge-doubling is never observed nor achievable. This behavior is also not accounted for by simply varying Γ in $\mathbf{T}_{\phi_f}(\alpha, \Gamma)$, and we must, therefore, extend our model.

Liquid crystals may be regarded as a continuous medium with a set of elastic constants. As such, the elastic continuum theory,[1] which we briefly review in Materials and Methods, has been an
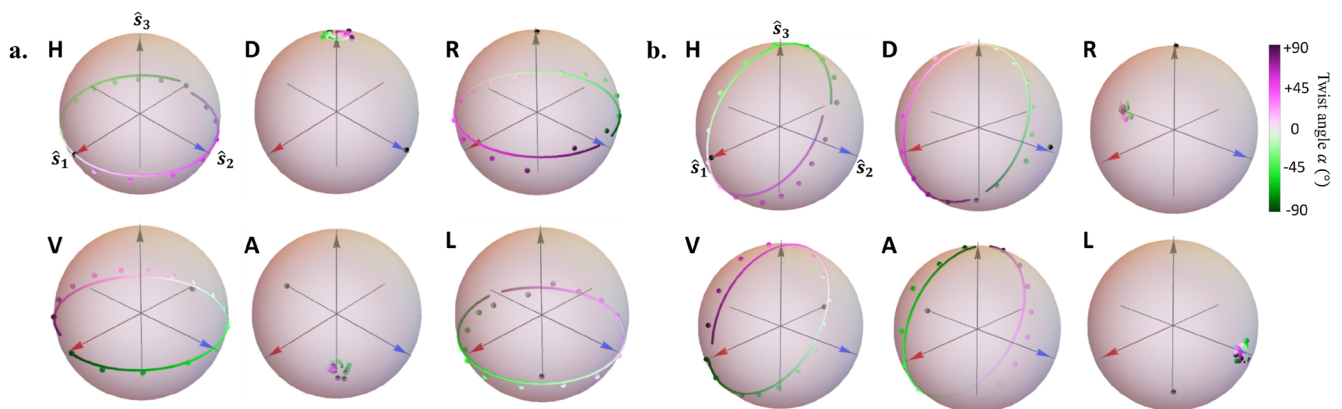
FIG. 3. Stokes vector reconstruction. Reconstructed average Stokes vectors in each of the 16 slices (colored points) for the cardinal input states (black points)—horizontal (H), vertical (V), diagonal (D), anti-diagonal (A), left-hand circular (L), and right-hand circular (R)—and theoretical fit (line) using the TNLC Jones matrix with $\Gamma_{fit} = 51.7$ for (a) DP(0, 1/2) and (b) DP(1/2, 0). The experimental Stokes vectors plotted are the average values in each slice of the discretized sample.
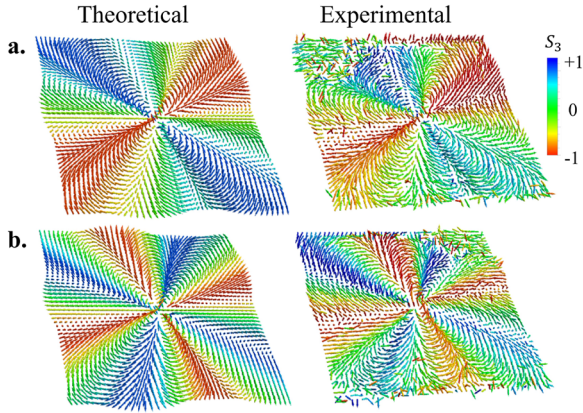
FIG. 4. Stokes vector reconstruction. For horizontally polarized input light, the theoretical and experimentally reconstructed local Stokes vectors (arrows) for (a) DP(1, 2) and (b) DP(2, 1). The arrow color is a measure of the local polarization's ellipticity, with left-hand circular as red, right-hand circular as blue, and linear as green.

excellent way to describe the influence of boundary conditions and externally applied fields—whether electric or magnetic—on these systems. Since liquid crystals are electrically polarizable, diamagnetic, and anisotropic in their electric/magnetic properties, an applied field will cause the molecules to align with the field direction. In general, the tilt and twist distributions of the liquid-crystal directors within the bulk become non-trivial and typically nonanalytical. These are determined by minimizing the Frank–Oseen free-energy density of the system.[26] The solution that arises is a coupled set of highly singular integrals to be solved simultaneously. In the high-voltage limit ($V/V_{T0} \geqslant 4$), certain approximations can be made to simplify solving these integrals around their singularities, with some analytical approximations when $V \gg V_{T0}$.[27] V_{T0} is the characteristic threshold voltage, or Freedericksz threshold, of the

system, dependent on material parameters; here, $V_{T0} = 0.966$ V or $V_{pp} = 2.733$ V. To analyze more general cases, we have opted to use a numerical minimization approach based on evolutionary methods, specifically a genetic algorithm, to also look at the response of the system for field strengths below the high-voltage limit. Remarkably, this method does not require any *a priori* hypothesis on the applied field. The details of our numerical approach will be found in a separate technical paper.[28]

With the numerically calculated tilt and twist distributions, the overall Jones matrix $\mathbf{J}_{\phi_f}(\alpha, V)$ is derived by multiplying together the N twisted liquid crystal cells of thickness d using the form of Eq. (4),

$$\mathbf{J}_{\phi_f}(\alpha, V) = \mathbf{R}(-\phi_b)\left[\prod_{j=0}^{N} \mathbf{M}_0(\alpha'(z_j), \Gamma(z_j))\right]\mathbf{R}(\phi_f), \qquad (10)$$

where $\alpha'(z_j) = \phi(z_{j+1}) - \phi(z_j)$, $z_j = jd$, $\phi_f = \phi(0)$ and $\phi_b = \phi(L)$ are the front and back alignment angles, respectively, and $\alpha = \phi(L) - \phi(0)$ is the total twist angle. The phase retardation $\Gamma(z_j)$ within the jth slice is calculated from the tilt distribution $\theta(z)$ using the trapezoidal rule in favor of left or right Riemann sums for a better estimate,

$$\Gamma(z_j) = \frac{\pi \Delta n d}{\lambda}\left[\cos^2 \theta(z_{j+1}) + \cos^2 \theta(z_j)\right]. \qquad (11)$$

A cell thickness of $L = 35 \, \mu m$ is used, with $N = 100$ slices for $d = L/N$. Figure 5(b) compares the experimentally reconstructed Stokes data for DP(0, 1/2) and horizontally polarized input light with numerical predictions (see the supplementary material figures for a 2D plot of this comparison).

This model reproduces quite accurately the experimental results. This would not be possible by simply assuming a linear twist distribution and varying Γ. In particular, the non-linear twist distributions account for the peculiar phenomenon of the evolving topological charge shown in Fig. 5(a). Further investigations will
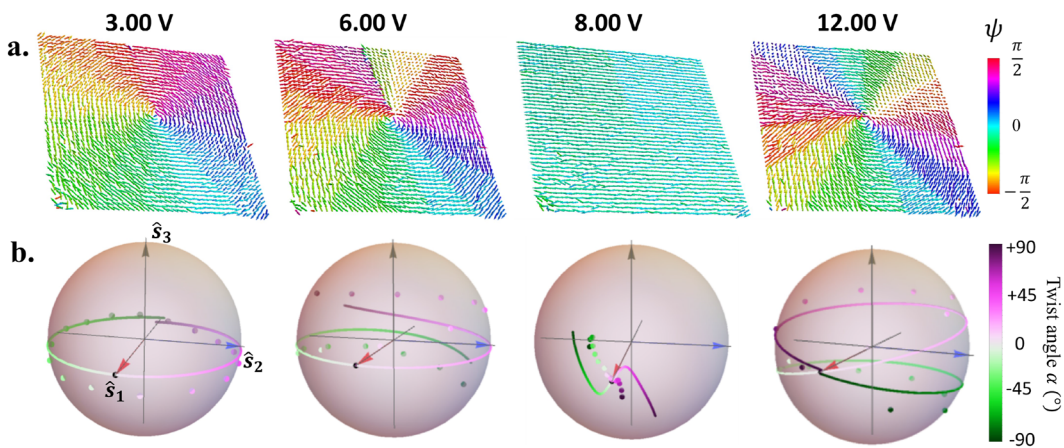
FIG. 5. Externally applied voltage on DP(0, 1/2). (a) Reconstructed local Stokes vectors (arrow) from a horizontally polarized input for voltage: V_{pp} = 3.00, 6.00, 8.00, and 12.00 V. The color corresponds to the polarization ellipse angle ψ with respect to the horizontal. (b) The experimental data (dots) are the output Stokes vectors, and the fits (lines) correspond to the theoretical curves obtained from the nematic liquid crystal twist and tilt distributions extracted from our genetic algorithm.

be required to determine if we achieve an actual evolution of the topological charge for the continuous version of DP(0, 1/2).

DISCUSSION AND CONCLUSIONS

We have shown the versatility of patterned twisted nematic cells, focusing on the action of dual q-plates on polarized light. The case in which no external field is applied has been analyzed in detail, and an analytic Jones matrix description of the dual-plates has been derived. We demonstrated that one can observe different functionalities depending on the effective retardation Γ or the plate orientation. It must be noted that Γ can either be fixed or tuned by means of temperature control.[29] Another way of controlling the effective retardation is via an applied field. However, in the case of dual-plates, an external field introduces additional deformations in the liquid-crystal medium, which affects the overall distribution of the molecular director. As a consequence, the resulting Jones matrix can be much more complicated.

At the same time, this can lead to intriguing unexpected effects, for instance, the generation of polarization patterns with apparent topologies, which depend on the applied voltage. Typically, a change in topology induced by a continuous parameter is associated with the existence of an intermediate critical point. However, we observe that dual q-plates always exhibit singular lines in the liquid-crystal orientation pattern, which are transferred to the polarization distribution of the transmitted light. Accordingly, no topological charge can be rigorously associated with the polarization distribution. Nevertheless, the observed patterns display distinguishable features, such as lemon and azimuthal patterns.

The main advantage of this technology is the possibility of accessing an entire family of vector beams through a single spin–orbit liquid-crystal device, contrary to the standard approach requiring multiple cascaded plates. Dual-plates thus provide a compact and efficient solution to the generation of complex vector beams, which proved to be a powerful resource for metrological[11,30] and high-dimensional quantum information protocols.[31] Dual-plates open a new avenue for optical functionalities based on liquid crystals. Here, we focused on plates with different topological structures patterned on the two alignment layers. Other possibilities will include dual Fresnel lenses, axicons, gratings, and magic windows. The use of these structures will also allow novel

studies and realizations of devices introducing 3D geometric phases.[32] In principle, the technology of dual-plates is not limited to liquid crystals. Femtosecond-laser writing in glass,[33–35] cascaded metasurfaces,[36] and two-photon polymerization[37] have all demonstrated the ability to create three-dimensional birefringent structures, which could potentially expand the application of dual-plates to smaller integrated systems.

MATERIALS AND METHODS

Fabrication

The process to fabricate dual-plates is similar to that for q-plates.[9,38] First, we start with two glass substrates, each with a conductive layer of indium tin oxide (ITO). A drop of an azobenzene-based dye (PAAD-22, provided by BEAM Co.) is deposited on top of the ITO; the sample is then spin-coated for 30 s at 4000 rpm and baked at 120° for 5 min. When exposed to the light of a wavelength around the peak of the azodye's absorption spectrum, the molecules will photoalign themselves according to the light linear polarization. Here, we use a 430-nm laser. Figure 6(a) shows the setup to pattern the sample. In particular, a digital micromirror device (DLP3000 DLP® 0.3 WVGA Series 220 DMD) is programmed to reflect a tailored intensity pattern. The resolution of the DMD is 608 x 684 with a micromirror pitch of 7.6 μm. A HWP can then be rotated to adjust the polarization to the required orientation. When fabricating q-plates, the two glass substrates are first glued together—with spacers between them to create a uniform cavity for the liquid crystals—and, then, the sample is exposed with the desired pattern. For dual-plates, each substrate is separately exposed with the front and back plate patterns, respectively. First, one substrate is laid flat, polymer layer up; next, the spacers are placed across the surface, followed by a drop of nematic liquid crystals (here, 6CHBT) in the center. For the samples presented here, silica microspheres with diameters between 32 and 38 μm are used as the spacers. The second substrate is laid on top, polymer layer down, and a fast-drying epoxy is applied to two edges. Note that the two substrates are glued with a lateral offset such that wires can be soldered to the conductive ITO layer; this will allow for a voltage to be applied across the sample. While the epoxy glue dries, the intensity pattern is observed between crossed polarizers while illuminated with white light. During this time, ~10–15 min, it is possible to alter the intensity pattern by gently sliding the glasses
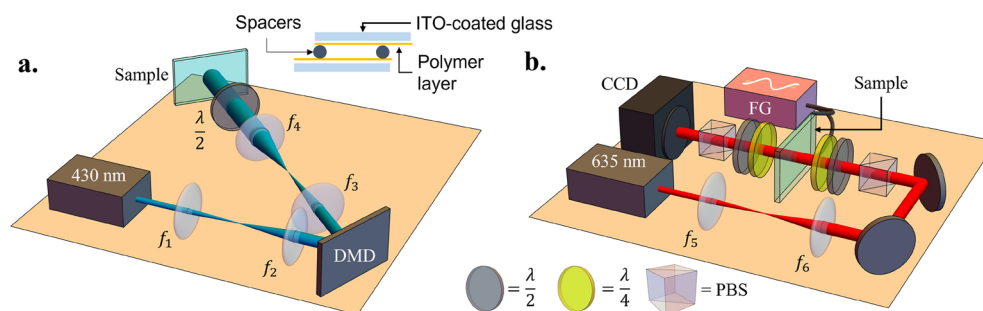
FIG. 6. Experimental setups. (a) Setup to pattern the glass plates for fabricating liquid-crystal devices. The inset shows the cross section of the constructed LC cell. (b) Setup to characterize the fabricated samples. DMD = digital micromirror device, PBS = polarizing beam splitter, and FG = function generator.
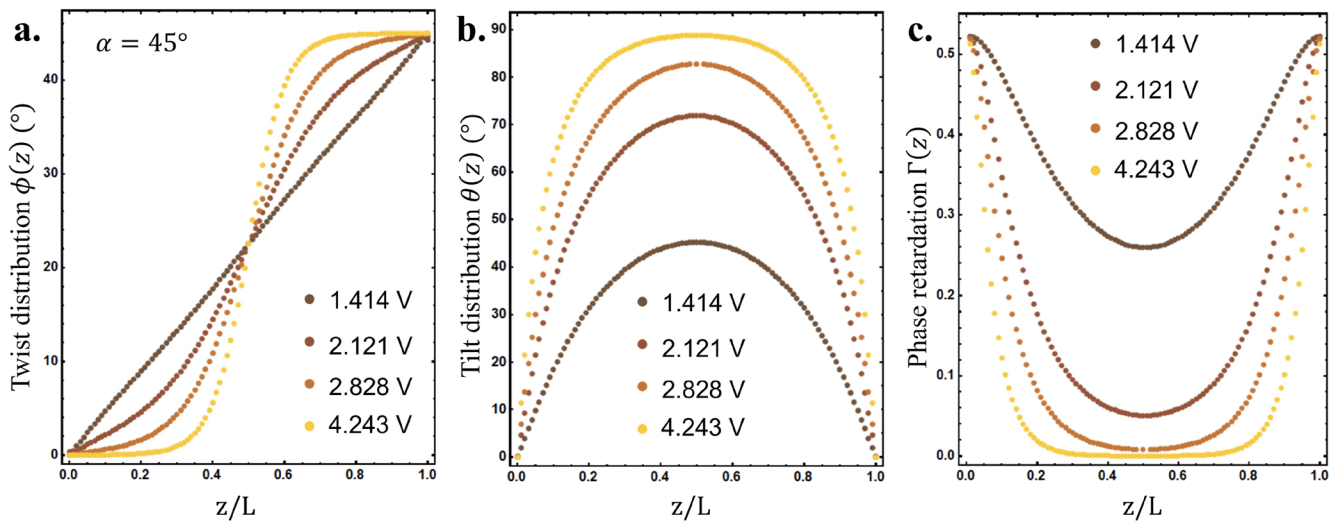
FIG. 7. Numerical optimization results for $\alpha = 45°$. (a) Twist and (b) tilt distributions for V = 1.141, 2.121, 2.828, and 4.243 V. (c) Phase retardation distribution $\Gamma(z)$ computed using $L = 35 \ \mu m$.

with respect to each other. When the patterns are not aligned, two singularities will be visible. The distance between the two singularities is minimized as much as possible, limited by the resolution of the eyesight of the person assembling the sample. In this proof-of-principle work, the alignment was carried out without the use of a microscope, yielding a residual separation of slightly less than 0.5 mm. However, higher-quality samples can be fabricated with the aid of microscopes and precision controls. Finally, the rest of the liquid crystals are injected into the cavity and the remaining sides of the cell are sealed off with glue. The completed sample is heated to ~100°C on a hot plate and cooled to room temperature once more to cement the alignment of the liquid crystals with the written patterns.

The setup to characterize the fabricated sample is shown in Fig. 6(b). A red 635-nm diode laser is used to illuminate the sample; it is expanded using a telescoping lens system to completely cover the patterned area. A polarizing beam splitter (PBS), a half-wave plate (HWP), and a quarter-wave plate (QWP) are used to prepare the input polarization state. A second set of QWP, HWP, and PBS is used to project the output polarization state from the sample onto a different polarization state. Another telescoping lens system (not shown) is used to image the sample plane and shrink the beam down to fit onto a CCD camera in order to record the intensity measurement. A function generator (FG) applies a sinusoidal waveform with 4 kHz frequency and peak-to-peak voltages V_{pp}—i.e., the difference between the maximum positive voltage and the minimum negative voltage of the waveform—between 0 and 20 V to the prepared sample. Polarization state tomography is thus performed for the six cardinal polarizations as inputs on the sample. This consists of projecting the output polarization state onto the six cardinal states and recording the intensity using the CCD camera, i.e., there are six measurements for each input state, for 36 measurements (images) total per configuration of the sample.

Elastic continuum theory

In order to determine the twist $\phi(z)$ and tilt $\theta(z)$ distributions of the liquid crystal director $\hat{\mathbf{n}}$ within a general sample, it is necessary to minimize the free energy of the system, given by the fundamental elastic continuum equation,

$$\mathcal{F} = \frac{1}{2}\left\{K_1\left[\nabla \cdot \hat{\mathbf{n}}(\mathbf{r})\right]^2 + K_2\left[\hat{\mathbf{n}}(\mathbf{r}) \cdot \nabla \times \hat{\mathbf{n}}(\mathbf{r})\right]^2 \right. \\ \left. + K_3\left[\hat{\mathbf{n}}(\mathbf{r}) \times \nabla \times \hat{\mathbf{n}}(\mathbf{r})\right]^2 - \mathbf{D} \cdot \mathbf{E} - \mathbf{B} \cdot \mathbf{H}\right\}, \quad (12)$$

over its volume. The K_i correspond to the elastic constants for the splay, twist, and bend distortions, respectively. For 6CHBT nematic liquid crystals, the elastic constants are $K_1 = 6.7$ pN, $K_2 = 3.4$ pN, and $K_3 = 10.6$ pN.[25] In the current case, where the back alignment layer is twisted by α with respect to the front layer, a coupled set of integrals must be solved numerically to find $\phi(z)$ and $\theta(z)$.[26] For completeness, we report the integrals here. The twist distribution $\phi(z)$ is given by

$$\phi(z) = \beta \int_0^{\theta(z)} \frac{\sqrt{1 + \kappa \sin^2\theta}}{g(\theta)\cos^2\theta(1 + \tau\sin^2\theta)} \, d\theta, \quad (13)$$

where $\kappa = (K_3 - K_1)/K_1$ and β is an unknown constant of integration to be determined from boundary conditions. The tilt distribution $\theta(z)$ is determined implicitly through

$$\frac{z}{L} = \frac{1}{2}\int_0^{\theta(z)} \frac{\sqrt{1 + \kappa\sin^2\theta}}{g(\theta)} \, d\theta \bigg/ \int_0^{\theta_m} \frac{\sqrt{1 + \kappa\sin^2\theta}}{g(\theta)} \, d\theta, \quad (14)$$

where $\theta_m \equiv \theta_m(V)$ is the maximum tilt angle located at $z = L/2$ and is itself a function of the applied field. The $g(\theta)$ function depends on β and θ_m, with the form

$$g(\theta) = \left\{ \frac{\sin^2\theta_m - \sin^2\theta}{(1 + \gamma\sin^2\theta)(1 + \gamma\sin^2\theta_m)} + \beta^2 \frac{1+\kappa}{1+\tau} \right.$$
$$\left. \times \left(\frac{1}{(1 + \tau\sin^2\theta_m)\cos^2\theta_m} - \frac{1}{(1 + \tau\sin^2\theta)\cos^2\theta} \right) \right\}^{1/2}, \quad (15)$$

where $\gamma = (\epsilon_\parallel - \epsilon_\perp)/\epsilon_\perp$ and $\tau = (K_3 - K_2)/K_2$. Here, $\epsilon_\parallel$ $(\epsilon_\perp)$ denotes the dielectric constant per unit volume that is parallel (perpendicular) to the local director.

We implemented a genetic algorithm to numerically determine the twist and tilt distributions. Figure 7 reports an example of the calculated distributions for a maximum twist angle of $\alpha = 45°$. Further details on our numerical routine will be found in Ref. 28.

SUPPLEMENTARY MATERIAL

We refer to the supplementary online material for a 2D visualization of the data presented in Figs. 4 and 5.

ACKNOWLEDGEMENTS

AUTHOR DECLARATIONS

Conflict of Interest

The authors have no conflicts to disclose.

Author Contributions

Alicia Sit: Conceptualization (equal); Data curation (equal); Formal analysis (equal); Investigation (equal); Methodology (equal); Software (equal); Validation (equal); Writing – original draft (equal); Writing – review & editing (equal). **Francesco Di Colandrea**: Investigation (equal); Methodology (equal); Software (equal); Supervision (equal); Validation (equal); Writing – review & editing (equal). **Alessio D'Errico**: Investigation (equal); Methodology (equal); Software (equal); Validation (equal); Writing – review & editing (equal). **Ebrahim Karimi**: Conceptualization (equal); Formal analysis (equal); Funding acquisition (equal); Investigation (equal); Methodology (equal); Software (equal); Supervision (equal); Validation (equal); Writing – review & editing (equal).

DATA AVAILABILITY

The data that support the findings of this study are available from the corresponding author upon reasonable request.

REFERENCES

[1] P. G. De Gennes and J. Prost, in *The Physics of Liquid Crystals*, 2nd ed. (Clarendon Press, Oxford, 1993).

[2] I. A. Shanks, "The physics and display applications of liquid crystals," Contemp. Phys. **23**, 65 (1982).

[3] M. Schadt, "The twisted nematic effect: Liquid crystal displays and liquid crystal materials," Mol. Cryst. Liq. Cryst. Incorporating Nonlinear Opt. **165**, 405 (1988).

[4] P. Yeh and C. Gu, *Optics of Liquid Crystal Displays* (John Wiley&Sons, 2009), Vol. 67.

[5] C. Gooch and H. Tarry, "The optical properties of twisted nematic liquid crystal structures with twist angles 90 degrees," J. Phys. D: Appl. Phys. **8**, 1575 (1975).

[6] H. L. Ong, "Optical properties of general twisted nematic liquid-crystal displays," Appl. Phys. Lett. **51**, 1398 (1987).

[7] E. Brasselet, N. Murazawa, H. Misawa, and S. Juodkazis, "Optical vortices from liquid crystal droplets," Phys. Rev. Lett. **103**, 103903 (2009).

[8] L. Marrucci, E. Karimi, S. Slussarenko, B. Piccirillo, E. Santamato, E. Nagali, and F. Sciarrino, "Spin-to-orbital conversion of the angular momentum of light and its classical and quantum applications," J. Opt. **13**, 064001 (2011).

[9] A. Rubano, F. Cardano, B. Piccirillo, and L. Marrucci, "Q-Plate technology: A progress review [invited]," J. Opt. Soc. Am. B **36**, 70 (2019).

[10] L. Yan, P. Gregg, E. Karimi, A. Rubano, L. Marrucci, R. W. Boyd, and S. Ramachandran, "Q-plate enabled spectrally diverse orbital-angular-momentum conversion for stimulated emission depletion microscopy," Optica **2**, 900 (2015).

[11] V. D'Ambrosio, N. Spagnolo, L. Del Re, S. Slussarenko, Y. Li, L. C. Kwek, L. Marrucci, S. P. Walborn, L. Aolita, and F. Sciarrino, "Photonic polarization gears for ultra-sensitive angular measurements," Nat. Commun. **4**, 2432 (2013).

[12] E. Karimi, L. Marrucci, C. de Lisio, and E. Santamato, "Time-division multiplexing of the orbital angular momentum of light," Opt. Lett. **37**, 127 (2012).

[13] A. Sit, F. Bouchard, R. Fickler, J. Gagnon-Bischoff, H. Larocque, K. Heshami, D. Elser, C. Peuntinger, K. Günther, B. Heim, C. Marquardt, G. Leuchs, R. W. Boyd, and E. Karimi, "High-dimensional intracity quantum cryptography with structured photons," Optica **4**, 1006 (2017).

[14] F. Cardano, F. Massa, H. Qassim, E. Karimi, S. Slussarenko, D. Paparo, C. de Lisio, F. Sciarrino, E. Santamato, R. W. Boyd, and L. Marrucci, "Quantum walks and wavepacket dynamics on a lattice with twisted photons," Sci. Adv. **1**, e150087 (2015).

[15] M. Stalder and M. Schadt, "Linearly polarized light with axial symmetry generated by liquid-crystal polarization converters," Opt. Lett. **21**, 1948 (1996).

[16] F. Cardano, E. Karimi, S. Slussarenko, L. Marrucci, C. de Lisio, and E. Santamato, "Polarization pattern of vector vortex beams generated by q-plates with different topological charges," Appl. Opt. **51**, C1 (2012).

[17] G. P. Crawford, J. N. Eakin, M. D. Radcliffe, A. Callan-Jones, and R. A. Pelcovits, "Liquid-crystal diffraction gratings using polarization holography alignment techniques," J. Appl. Phys. **98**, 123102 (2005).

[18] C. Provenzano, P. Pagliusi, and G. Cipparrone, "Electrically tunable two-dimensional liquid crystals gratings induced by polarization holography," Opt. Express **15**, 5872 (2007).

[19] I. Nys, B. Berteloot, and K. Neyts, "Photoaligned liquid crystal devices with switchable hexagonal diffraction patterns," Materials **15**, 2453 (2022).

[20] J. Kobashi, H. Yoshida, and M. Ozaki, "Planar optics with patterned chiral liquid crystals," Nat. Photonics **10**, 389 (2016).

[21] C. A. Valagiannopoulos, M. Mattheakis, S. N. Shirodkar, and E. Kaxiras, "Manipulating polarized light with a planar slab of black phosphorus," J. Phys. Commun. **1**, 045003 (2017).

[22] C. Valagiannopoulos, "Electromagnetic analog to magic angles in twisted bilayers of two-dimensional media," Phys. Rev. Appl. **18**, 044011 (2022).

[23] M. Yamauchi, "Jones-matrix models for twisted-nematic liquid-crystal devices," Appl. Opt. **44**, 4484 (2005).

[24] A. Yariv and P. Yeh, *Optical Waves in Crystals: Propagation and Control of Laser Radiation* (Wiley-Interscience, 2003).

[25] E. Nowinowski-Kruszelnicki, J. Kedzierski, Z. Raszewski, L. Jaroszewicz, M. A. Kojdecki, W. Piecek, P. Perkowski, M. Olifierczuk, E. Miszczyk, K. Ogrodnik, and P. Morawiak, "Measurement of elastic constants of nematic liquid crystals with use of hybrid in-plane-switched cell," Opto-Electron. Rev. **20**, 255 (2012).

07 December 2024 15:55:02

[26] H. J. Deuling, "Deformation pattern of twisted nematic liquid crystal layers in an electric field," Mol. Cryst. Liq. Cryst. **27**, 81 (1974).

[27] T. W. Preist, K. R. Welford, and J. R. Sambles, "Response of a twisted nematic liquid crystal to any applied potential," Liq. Cryst. **4**, 103 (1989).

[28] A. Sit, F. Di Colandrea, A. D'Errico, and E. Karimi, "A genetic algorithm for the response of twisted nematic liquid crystals to an applied field," Phys. Rev. E (in press); arXiv:240300948 (2024).

[29] E. Karimi, B. Piccirillo, E. Nagali, L. Marrucci, and E. Santamato, "Efficient generation and sorting of orbital angular momentum eigenmodes of light by thermally tuned q-plates," Appl. Phys. Lett. **94**, 231124 (2009).

[30] F. K. Fatemi, "Cylindrical vector beams for rapid polarization-dependent measurements in atomic systems," Opt. Express **19**, 25143 (2011).

[31] Z.-X. Li, Y.-P. Ruan, P. Chen, J. Tang, W. Hu, K.-Y. Xia, and Y.-Q. Lu, "Liquid crystal devices for vector vortex beams manipulation and quantum information applications [Invited]," Chin. Opt. Lett. **19**, 112601 (2021).

[32] S. Slussarenko, A. Alberucci, C. P. Jisha, B. Piccirillo, E. Santamato, G. Assanto, and L. Marrucci, "Guiding light via geometric phases," Nat. Photonics **10**, 571 (2016).

[33] S. Nolte, M. Will, J. Burghoff, and A. Tuennermann, "Femtosecond waveguide writing: A new avenue to three-dimensional integrated optics," Appl. Phys. A: Mater. Sci. Process. **77**, 109 (2003).

[34] P. Yang, G. R. Burns, J. Guo, T. S. Luk, and G. A. Vawter, "Femtosecond laser-pulse-induced birefringence in optically isotropic glass," J. Appl. Phys. **95**, 5280 (2004).

[35] L. A. Fernandes, J. R. Grenier, P. R. Herman, J. S. Aitchison, and P. V. S. Marques, "Femtosecond laser writing of waveguide retarders in fused silica for polarization control in optical circuits," Opt. Express **19**, 18294 (2011).

[36] C. Pfeiffer and A. Grbic, "Cascaded metasurfaces for complete phase and polarization control," Appl. Phys. Lett. **102**, 231116 (2013).

[37] V. Tribuzi, R. D. Fonseca, D. S. Correa, and C. R. Mendonça, "Birefringent microstructures fabricated by two-photon polymerization containing anazopolymer," Opt. Mater. Express **3**, 21 (2013).

[38] H. Larocque, J. Gagnon-Bischoff, F. Bouchard, R. Fickler, J. Upham, R. W. Boyd, and E. Karimi, "Arbitrary optical wavefront shaping via spin-to-orbit coupling," J. Opt. **18**, 124002 (2016).

07 December 2024 15:55:02